





# Kinetic Cascade in Solar-wind Turbulence: 3D3V Hybrid-kinetic Simulations with Electron Inertia

Silvio Sergio Cerri<sup>1</sup> , Sergio Servidio<sup>2</sup> , and Francesco Califano<sup>1</sup> 

<sup>1</sup> Dipartimento di Fisica “E. Fermi,” Università di Pisa, Largo B. Pontecorvo 3, I-56127 Pisa, Italy; [silvio.sergio@df.unipi.it](mailto:silvio.sergio@df.unipi.it)

<sup>2</sup> Dipartimento di Fisica, Università della Calabria, I-87036 Rende (CS), Italy

Received 2017 July 25; revised 2017 August 18; accepted 2017 August 21; published 2017 September 5

## Abstract

Understanding the nature of the turbulent fluctuations below the ion gyroradius in solar-wind (SW) turbulence is a great challenge. Recent studies have been mostly in favor of kinetic Alfvén wave (KAW)-type fluctuations, but other kinds of fluctuations with characteristics typical of magnetosonic, whistler, and ion-Bernstein modes could also play a role depending on the plasma parameters. Here, we investigate the properties of the subproton-scale cascade with high-resolution hybrid-kinetic simulations of freely decaying turbulence in 3D3V phase space, including electron inertia effects. Two proton plasma beta are explored: the “intermediate”  $\beta_p = 1$  and “low”  $\beta_p = 0.2$  regimes, both typically observed in the SW and corona. The magnetic energy spectrum exhibits  $k_{\perp}^{-8/3}$  and  $k_{\parallel}^{-7/2}$  power laws at  $\beta_p = 1$ , while they are slightly steeper at  $\beta_p = 0.2$ . Nevertheless, both regimes develop a spectral anisotropy consistent with  $k_{\parallel} \sim k_{\perp}^{2/3}$  at  $k_{\perp} \rho_p > 1$  and pronounced small-scale intermittency. In this context, we find that the kinetic-scale cascade is dominated by KAW-like fluctuations at  $\beta_p = 1$ , whereas the low- $\beta$  case presents a more complex scenario suggesting the simultaneous presence of different types of fluctuations. In both regimes, however, a possible role of the ion-Bernstein-type fluctuations at the smallest scales cannot be excluded.

*Key words:* methods: numerical – plasmas – solar wind – turbulence

## 1. Introduction

Nearly all astrophysical and space plasmas are in a turbulent state. In this context, the solar wind (SW) represents an ideal environment for studying collisionless plasma turbulence from the magnetohydrodynamic (MHD) range down to kinetic scales (Bruno & Carbone 2013; Chen 2016). Increasingly accurate in situ measurements of SW turbulence down to electron scales have been available over the past years (Bale et al. 2005; Alexandrova et al. 2008; Sahraoui et al. 2010; He et al. 2012; Chen et al. 2013; Roberts et al. 2013), showing the presence of breaks in the electromagnetic fluctuations at kinetic scales. In the proton kinetic range, for instance, the typical slope for the magnetic energy spectrum is found to be between  $-2.5$  and  $-3$ , i.e., steeper than the correspondent spectrum at MHD scales, while the electric spectrum becomes simultaneously shallower below the proton gyroradius scale. A wide number of theoretical models (Vainshtein 1973; Galtier & Bhattacharjee 2003; Cho & Lazarian 2004; Howes et al. 2008; Schekochihin et al. 2009; Boldyrev & Perez 2012; Boldyrev et al. 2013; Passot & Sulem 2015) and numerical investigations (Shaikh & Zank 2009; Valentini et al. 2010; Howes et al. 2011; Servidio et al. 2012, 2014; Franci et al. 2015, 2016; Told et al. 2015; Sulem et al. 2016; Cerri et al. 2016; Groselj et al. 2017) have been exploited in order to explain the observed behavior of SW turbulent spectra, mostly in terms of the properties of fluctuations derived from wave physics. In this context, the observed spectra at kinetic scales are usually interpreted as a cascade of kinetic Alfvén waves (KAWs) and/or of higher-frequency waves, such as magnetosonic (MS), whistler waves (WW), and/or ion-Bernstein (IB) modes. Most of the SW observations point toward a cascade of KAW-like fluctuations at  $\beta \sim 1$  (Sahraoui et al. 2010; He et al. 2012; Chen et al. 2013; Roberts et al. 2013), where  $\beta$  is the ratio between thermal and magnetic pressures, although whistler-like turbulence have also

been observed (Narita et al. 2011, 2016b). In fact, theoretical arguments suggest that different kinds of fluctuations could coexist and interact, depending on the plasma parameters (Stawicki et al. 2001; Gary & Smith 2009; Mithaiwala et al. 2012; Podesta 2012). This idea has been recently explored via 2D numerical simulations that suggested an increasingly KAW-like turbulence as  $\beta$  increases, whereas a more complex scenario—i.e., a mixture of different kind of fluctuations, including KAW-like ones—seems to emerge in the low- $\beta$  regimes (Cerri et al. 2016, 2017; Groselj et al. 2017). However, interpreting the turbulent cascade only in terms of wave physics is perhaps limiting and unsatisfactory (Matthaeus et al. 2014). Recently, the idea that magnetic reconnection can play a fundamental role in the formation of the small-scale spectrum has emerged (Cerri & Califano 2017; Franci et al. 2017; Loureiro & Boldyrev 2017; Mallet et al. 2017). These interpretations are somewhat at odds with the picture of turbulence made solely by a cascade of waves, as pointed out also by the intermittent behavior of SW turbulence (Sorriso-Valvo et al. 1999; Perri et al. 2012; Kiyani et al. 2013; Osman et al. 2014).

In this Letter, we present high-resolution 3D3V simulations of the turbulent cascade below the proton gyroradius within a hybrid Vlasov–Maxwell (HVM) model of plasma including finite electron inertia ( $m_p/m_e = 100$ ). Here, we focus on the spectral and intermittent properties of kinetic-scale turbulence in order to address the question of a possible dependence of the physics of such cascade on the plasma beta parameter. We note that our hybrid approach, although not retaining all the electron kinetic effects, fully captures the ion kinetic physics and allows for KAW, magnetosonic, whistler, and ion-Bernstein fluctuations to be present. We want to stress that here we analyze the properties of the turbulent fluctuations and we relate them to the characteristic features of the corresponding linear modes, but in doing this we are not assuming that turbulence is made

by a sea of linear waves: the aim of the analysis is to understand and classify the characteristics of turbulent fluctuations in analogy with those derived via linear theory.

## 2. The HVM Model and Simulations Setup

The HVM model couples fully kinetic protons to fluid electrons through a generalized Ohm's law (Mangeney et al. 2002; Valentini et al. 2007). The model equations, normalized with respect to the proton characteristic quantities (mass  $m_p$ , gyrofrequency  $\Omega_p$ , and inertial length,  $d_p$ ) and to the Alfvén speed  $v_A$ , read

$$\frac{\partial f}{\partial t} + \mathbf{v} \cdot \frac{\partial f}{\partial \mathbf{x}} + (\mathbf{E} + \mathbf{v} \times \mathbf{B}) \cdot \frac{\partial f}{\partial \mathbf{v}} = 0, \quad (1)$$

$$(1 - d_e^2 \nabla_{\perp}^2) \mathbf{E} = -\mathbf{u} \times \mathbf{B} + \frac{\mathbf{J} \times \mathbf{B}}{n} - \frac{\nabla p_e}{n}, \quad (2)$$

$$\frac{\partial \mathbf{B}}{\partial t} = -\nabla \times \mathbf{E}, \quad \nabla \times \mathbf{B} = \mathbf{J}, \quad (3)$$

where  $f(\mathbf{x}, \mathbf{v}, t)$  is the proton distribution function,  $d_e^2 = m_e$  is the electron skin depth, quasi-neutrality  $n_p \simeq n_e \equiv n$  is assumed, and the displacement current is neglected in Ampère's law. In the generalized Ohm's law, the leading electron inertia term  $d_e^2 \nabla^2 \simeq d_e^2 \nabla_{\perp}^2$  has been included (assuming  $k_{\parallel}^2 \ll k_{\perp}^2$  and a naturally anisotropic cascade). An isothermal closure for the electron pressure,  $p_e = nT_{0,e}$ , is adopted, and number density,  $n$ , and proton mean velocity,  $\mathbf{u}$ , are computed as  $v$ -space moments of  $f$ .

We initialize the simulations with a Maxwellian proton distribution function with isotropic temperature  $T_{0,p}$  and an electron fluid with  $T_{0,e} = T_{0,p}$ , embedded in a uniform background magnetic field  $\mathbf{B}_0 = B_0 \mathbf{e}_z$  with  $B_0 = 1$ . We further impose initial random large-scale 3D isotropic magnetic perturbations,  $\mathbf{B} = \mathbf{B}_0 + \delta \mathbf{B}$ , with wavenumbers  $0.1 \leq kd_i \leq 0.5$  and  $\delta B^{\text{rms}} \simeq 0.23$ . We use  $384^2$  grid points in the perpendicular  $xy$ -plane and 64 points in the parallel  $z$ -direction, uniformly distributed to discretize a periodic simulation box with  $L_{\perp} = 10 \pi d_p$  and  $L_{\parallel} = 2L_{\perp} = 20 \pi d_p$ , corresponding to a perpendicular resolution  $\Delta x = \Delta y \simeq 0.08 d_p = 0.8 d_e$  and  $\Delta z \simeq d_p$ . This corresponds to a spectral domain that spans more than two decades in perpendicular wavenumbers,  $0.2 \leq k_{\perp} d_p \leq 38.4$ , and more than one decade in its parallel counterpart,  $0.1 \leq k_{\parallel} d_p \leq 3.2$ . We apply (weak) spectral filters during the simulation in order to prevent spurious numerical effects at the smallest scales (Lele 1992), thus determining a cutoff in the turbulent energy spectra for  $k_{\perp} d_p \gtrsim 20$  and for  $k_{\parallel} d_p \gtrsim 2$ . The velocity domain is limited in each direction by  $v_{\text{max}} = \pm 5 v_{\text{th},p}$  for the  $\beta_p = 1$  case and by  $v_{\text{max}} = \pm 8 v_{\text{th},p}$  for  $\beta_p = 0.2$ , with  $51^3$  and  $61^3$  uniformly distributed velocity grid points, respectively.

## 3. Anisotropy and Intermittency of Kinetic Turbulence

Within a few outer-scale nonlinear times the initial condition freely decays into a fully developed turbulent state at  $t = t_*$ . Such time is identified by a peak in the rms current density,  $J^{\text{rms}}$ . In order to increase the statistics, the spectral analysis of turbulent fluctuations presented here includes a short time average over  $\Delta t = 10 \Omega_p^{-1} \ll t_*$ , starting from  $t_*$ .

Before discussing the spectral properties, a difference between the  $\beta_p = 1$  and  $\beta_p = 0.2$  regimes is first pointed out at the level of the spatial structures emerging in the fully

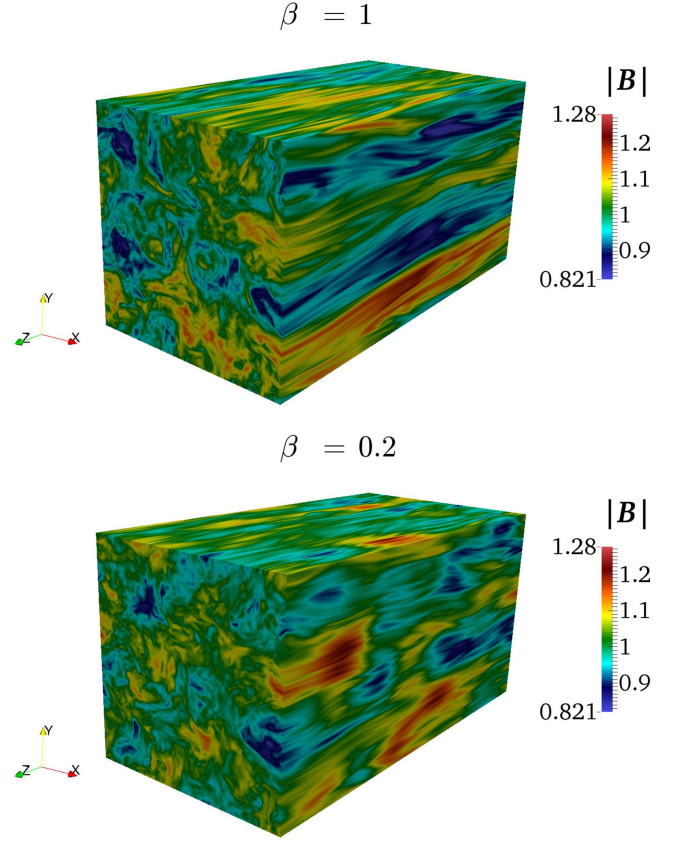


**Figure 1.** Three-dimensional representation of the magnetic field magnitude,  $|\mathbf{B}|$ , in the fully developed turbulent state for  $\beta_p = 1$  and  $\beta_p = 0.2$  regimes (top and bottom panels, respectively).

developed turbulent state. This is shown in Figure 1 where we draw the three-dimensional contours of the magnetic field magnitude at  $t = t_*$  in the two distinct regimes (top and bottom panels for  $\beta_p = 1$  and  $\beta_p = 0.2$ , respectively). As expected, starting with the same initially isotropic condition, in both cases the fluctuations gradually cascade into strongly anisotropic turbulence. However, while the  $\beta_p = 1$  regime exhibits perpendicular small-scale structures and very elongated fluctuations along  $\mathbf{B}_0$  that are typical of Alfvénic turbulence, the  $\beta_p = 0.2$  case presents shorter parallel structures that are instead reminiscent of magnetosonic fluctuations.

The spectral anisotropy of the turbulent fluctuations is shown in Figure 2, where we draw the two-dimensional energy spectrum of the total magnetic fluctuations,  $\delta B$  (top panels), and of the parallel electric fluctuations,  $\delta E_{\parallel}$  (bottom panels), for both regimes (left and right columns for  $\beta_p = 1$  and  $\beta_p = 0.2$ , respectively). Anisotropy is also observed at  $k\rho_p < 1$ , although this region contains few  $k$  points and is thus less relevant. At smaller scales,  $k_{\perp} \rho_p > 1$ , the anisotropy is instead evident: the turbulent cascade is mainly perpendicular to  $\mathbf{B}_0$  and the fluctuations seem to follow a  $k_{\parallel} \sim k_{\perp}^{2/3}$  pattern. This is more pronounced in the  $\beta_p = 1$  case, where the available sub-proton-scale range is larger than in the low- $\beta_p$  counterpart. Such pattern reveals a weaker anisotropy than the  $k_{\parallel} \sim k_{\perp}^{1/3}$  scaling phenomenologically expected for both KAW and whistler turbulence (Cho & Lazarian 2004; Schekochihin et al. 2009), and it is rather in agreement with the one predicted for turbulence mainly concentrated within 2D sheet-like

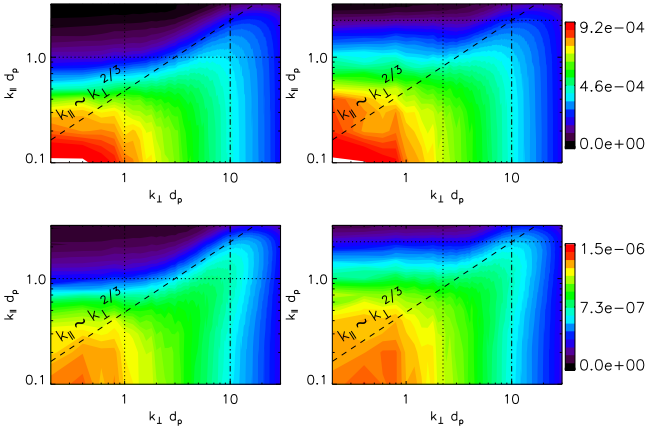


**Figure 2.** Two-dimensional energy spectrum in the  $(k_{\perp}, k_{\parallel})$  plane of the total magnetic fluctuations and of the parallel electric fluctuations,  $\mathcal{E}_B(k_{\perp}, k_{\parallel})$  and  $\mathcal{E}_{E\parallel}(k_{\perp}, k_{\parallel})$  (top and bottom rows, respectively) for  $\beta_i = 1$  (left column) and  $\beta_i = 0.2$  (right column).

structures (Boldyrev & Perez 2012). The spectra of fluctuations in the other quantities show the same behavior (not shown here).

A classical intermittency analysis has been performed on both simulations at about the peak of the nonlinear activity. In order to define the large-scale limit of the inertial range, we evaluated the perpendicular and parallel autocorrelation functions, respectively defined as  $C(r_{\perp}) = \langle \delta \mathbf{B}(\mathbf{x} + \mathbf{r}_{\perp}) \cdot \delta \mathbf{B}(\mathbf{x}) \rangle$  and  $C(r_{\parallel}) = \langle \delta \mathbf{B}(\mathbf{x} + \mathbf{r}_{\parallel}) \cdot \delta \mathbf{B}(\mathbf{x}) \rangle$  (Frisch 1995). We assumed isotropy in the perpendicular  $xy$ -plane, with the parallel direction along  $\mathbf{B}_0$ , i.e., along  $z$ . The  $e$ -folding length approximately gives the integral scale, which is about  $\lambda_{\perp} \sim 3d_p$  in the perpendicular direction (corresponding to  $k_{\perp} d_p \sim 2$ ), for both regimes. The situation is different in the parallel direction, where the parallel correlation length is  $\lambda_{\parallel} \sim 8d_p$  for  $\beta_p = 0.2$ , while it is  $\lambda_{\parallel} \sim 12d_p$  for  $\beta_p = 1$  (corresponding to  $k_{\parallel} d_p \sim 0.8$  and  $\sim 0.5$ , respectively). This is in qualitative agreement with the features spotted in Figure 1 and quantitatively with the corresponding spectra (see Figure 4), indicating differences already in the large-scale properties of the fluctuations possibly due to a different decorrelation mechanism along the mean field.

The level of intermittency can be better quantified by the probability distribution functions (PDFs) of the magnetic field increments at a given scale  $r$ , defined as

$$\Delta b_r \equiv [\delta \mathbf{B}(\mathbf{x} + \mathbf{r}) - \delta \mathbf{B}(\mathbf{x})] \cdot \hat{\mathbf{r}}. \quad (4)$$

We show here the statistics of the perpendicular increments, namely,  $r \equiv r_{\perp}$ , spanning this increment from lengths larger than the correlation scale  $\lambda_{\perp}$ , down to the smallest available scale ( $\Delta x \sim 0.08 d_p$ ). These distributions are reported in Figure 3(a) for the  $\beta_p = 0.2$  regime for three cases, namely,  $r/d_p = 21, 0.6$  and  $0.08$ . These PDFs, as expected, become increasingly intermittent going toward smaller scales. In order to compare among cases, and among different times, we measured the scale-dependent kurtosis  $\chi$ —the fourth-order moment of the increments in Equation (4)—that can be measured as

$$\chi = \frac{\langle \Delta b_r^4 \rangle}{\langle \Delta b_r^2 \rangle^2}. \quad (5)$$

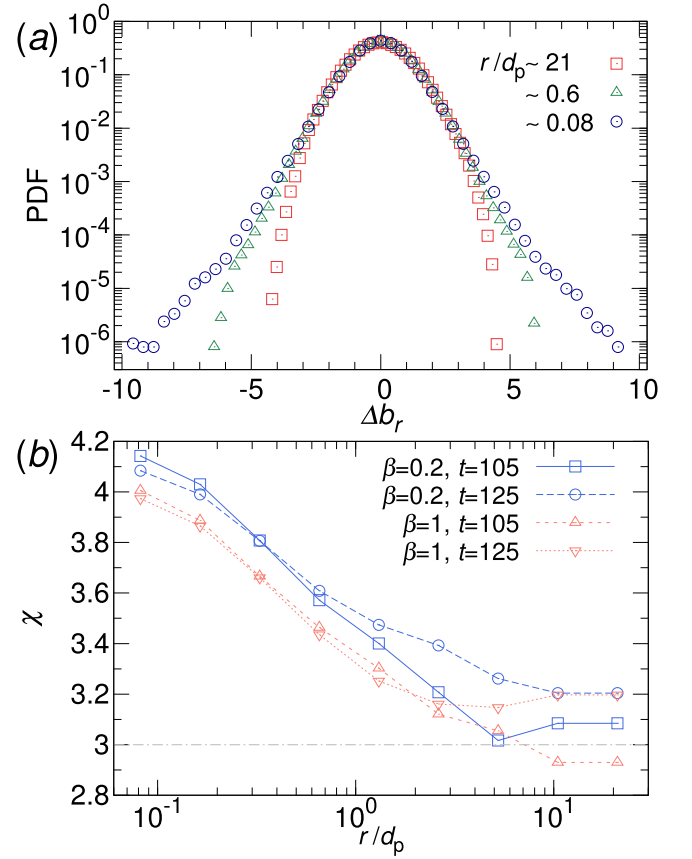


**Figure 3.** Top: PDFs of magnetic increments for  $\beta_p = 0.2$ , at different perpendicular lags. Bottom: scale-dependent kurtosis  $\chi$ . Comparison of the scale-dependent Kurtosis, at different times, for the two betas.

This quantity is reported in Figure 3(b), as a function of the perpendicular scale  $r$ , for the two values of  $\beta$ , at two distinct times. At large scales, for  $r > 5 d_p$ , the distribution becomes Gaussian, where  $\chi \sim 3$ , in agreement with the computation of the correlation lengths. At small scales, in the inertial range of turbulence, there is an enhancement due to the intermittent nature of the cascade, due to the presence of coherent structures and nonlinear waves. At the smallest scales, a saturation of the multifractality is observed, in agreement with observations in the SW. In fact, the study of high-order structure functions up to the sixth moment and of their exponents, shows deviation from monofractality (not shown here). Here, this process of saturation might also be slightly affected by the presence of artificial dissipation. It is important to note that at scales in the inertial-dispersive range, the case with  $\beta_p = 0.2$  is more intermittent than the  $\beta_p = 1$  regime, indicating a higher degree of coherency in the small-scale fluctuations.

#### 4. Spectral Features of Kinetic-scale Fluctuations

In Figure 4, we show the one-dimensional magnetic energy spectrum for both regimes (green and blue lines for  $\beta_p = 1$  and  $\beta_p = 0.2$ , respectively): the  $k_{\parallel}$ -averaged spectrum versus  $k_{\perp}$ ,  $\langle \mathcal{E}_B(k_{\perp}) \rangle_{k_{\parallel}}$  (top frame), and the  $k_{\perp}$ -averaged counterpart versus  $k_{\parallel}$ ,  $\langle \mathcal{E}_B(k_{\parallel}) \rangle_{k_{\perp}}$  (bottom frame). The average procedure, e.g.,  $\langle \mathcal{E}(k_{\perp}) \rangle_{k_{\parallel}}$ , here is defined as the summation of  $\mathcal{E}(k_{\parallel,i}, k_{\perp,j})$  over the points of the  $\{k_{\parallel,i}\}_{i=1, \dots, N_{\parallel}}$  grid, divided by those number of points,  $N_{\parallel}$ . Such a procedure, when specified, can be restricted

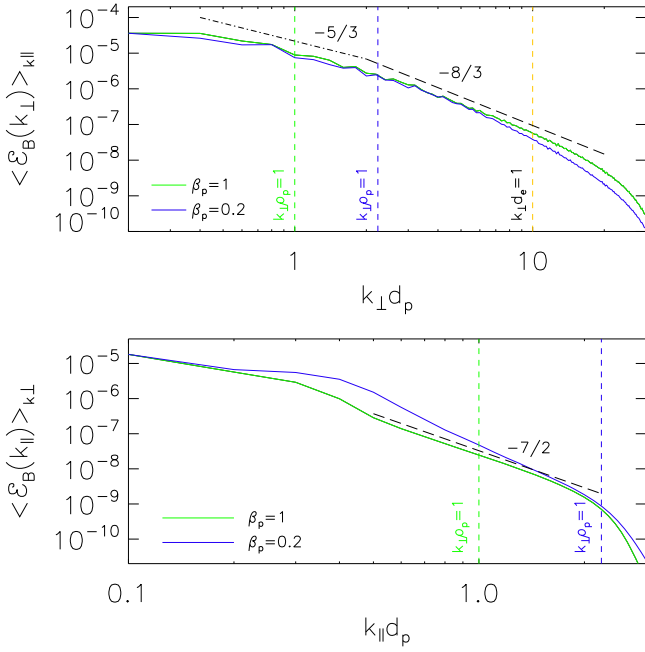


**Figure 4.** Total magnetic energy spectrum vs.  $k_\perp$  (top panel) and vs.  $k_\parallel$  (bottom panel), for  $\beta_i = 0.2$  and  $\beta_i = 1$  (blue and green lines, respectively).

to a  $k_\perp$ -dependent subset of points,  $n_\parallel(k_\perp)$ , of the entire  $k_\parallel$  grid (see below in this section). At large perpendicular scales,  $0.4 \lesssim k_\perp \rho_p \lesssim 2$ , a nearly  $-5/3$  power law is visible in both cases, although the MHD range is too limited to draw conclusions. At small perpendicular scales,  $k_\perp \rho_p \gtrsim 2$ , the  $\beta_p = 1$  regime exhibits a power law consistent with a  $-8/3$  slope (this has been verified through compensated spectra), while the  $\beta_p = 0.2$  case shows a steeper spectrum, close to  $k_\perp^{-3}$ . For small parallel wavenumbers, roughly  $k_\parallel \rho_p \lesssim 0.5$ , an excess of magnetic energy is present for  $\beta_p = 0.2$  and no clear power laws can be drawn for both regimes. For  $k_\parallel \rho_p \gtrsim 0.5$ , instead, a  $-7/2$  slope is observed at  $\beta_p = 1$ , whereas at lower  $\beta$  it is again steeper (roughly between  $k_\perp^{-9/2}$  and  $k_\perp^{-5}$ ). Note that the kinetic-range cascade, expected to take place at  $k \rho_p > 1$ , in the parallel wavenumbers already starts at  $k_\parallel \rho_p \sim 0.5$  due to the anisotropic nature of the turbulent cascade itself (cf. Figure 2). In particular, consistently with the spectral anisotropy and the intermittency analysis, the observed power laws for the magnetic spectrum at  $\beta_p = 1$ , i.e.,  $\propto k_\perp^{-8/3}$  and  $\propto k_\parallel^{-7/2}$ , are in agreement with those predicted in Boldyrev & Perez (2012).

A useful tool for the investigation of turbulent fluctuation properties are the spectral ratios of different quantities (Chen et al. 2013; Cerri et al. 2016, 2017; Chen & Boldyrev 2017; Groselj et al. 2017; Huang et al. 2017). Here, in order to highlight the characteristic behavior of small-scale fluctuations in the two different regimes, we consider the following quantities:

$$C_p \equiv \beta_p^2 \frac{\delta n^2}{\delta B_\parallel^2}, \quad C_A \equiv \frac{\delta E_\perp^2}{\delta B_\perp^2}, \quad C_\parallel \equiv \frac{\delta B_\parallel^2}{\delta B^2}, \quad (6)$$

where  $\tau \equiv T_{0,e}/T_{0,i} = 1$  already has been assumed in normalizing  $C_p$ . Let us relate them to the characteristic signatures that the main oblique modes would leave on the above ratios (Schechihin et al. 2009; Boldyrev et al. 2013). Since we are interested in the oblique fluctuations and given the anisotropic

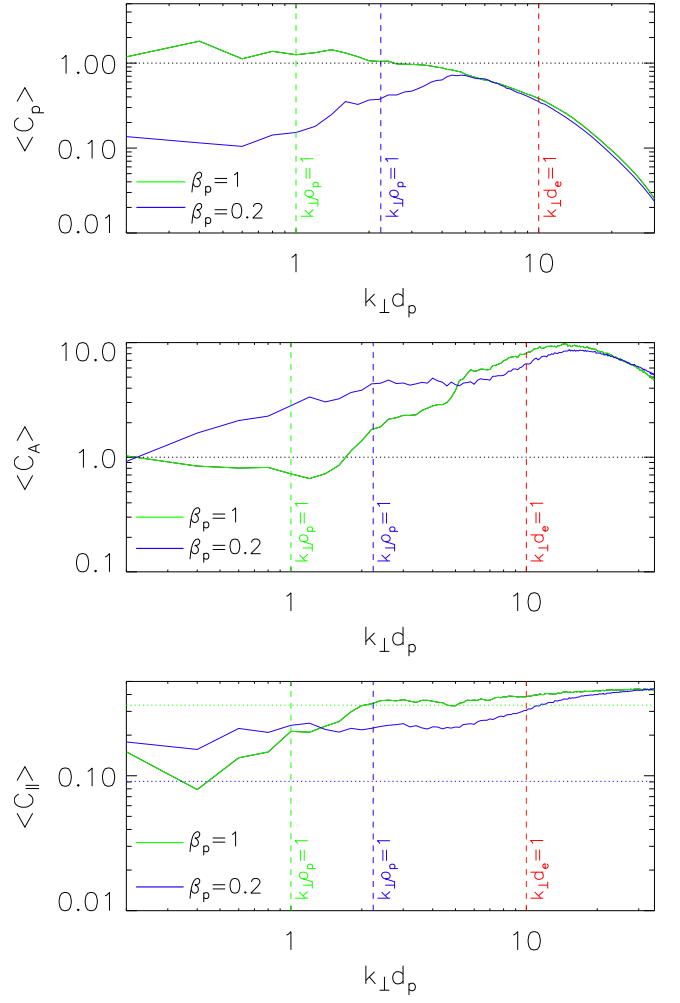


**Figure 5.** Averaged spectral ratios in Equation (6) vs.  $k_\perp$  for  $\beta_i = 0.2$  and  $\beta_i = 1$  (blue and green lines, respectively). The average has been taken over those  $k_\parallel$  such that  $k_\parallel \leq k_\perp^{2/3} \rho_p^{-1/3}$  (cf. Figure 2).

behavior of the turbulent energy cascade shown in Figure 2, the ratios defined above will be averaged over parallel wavenumbers such that  $k_\parallel \leq k_\perp^{2/3} \rho_p^{-1/3}$ . The resulting ratios are thus a function of  $k_\perp$  only, highlighting the properties of the main turbulent fluctuations and their connection with previous 2D numerical studies (Cerri et al. 2016, 2017; Groselj et al. 2017).

We first consider  $C_p$  (Figure 5, top panel): the normalized ratio between density and parallel magnetic fluctuations is expected to be unity,  $C_p \approx 1$ , for low-frequency Alfvénic/KAW fluctuations, whereas higher-frequency modes such as MS, WW, and IB should leave this ratio much smaller, namely,  $C_p \ll 1$ . For  $\beta_p = 1$ , the  $C_p$  ratio is about unity in nearly all the  $k_\perp$  range, which is a signature of turbulence dominated by low-frequency Alfvénic/KAW-like fluctuations. In the  $\beta_p = 0.2$  case, instead, we obtain  $C_p \ll 1$  at large scales,  $k_\perp \rho_p < 1$ , and it then increases for  $k_\perp \rho_p > 1$ , reaching values similar to those observed at  $\beta_p = 1$ . In both regimes, the behavior of  $C_p$  at the smallest scales,  $k_\perp d_p \gg 1$ , is most likely due to a combined effect of  $k_\perp d_e$  terms (Chen & Boldyrev 2017) and by the enhanced coupling of the MS, WWs, and KAWs with the ion-Bernstein branches in the oblique electromagnetic case (Podesta 2012).

Second, we consider  $C_A$  (Figure 5, middle panel): at  $k_{\perp} \rho_p < 1$ , this ratio is expected to be unity for Alfvénic fluctuations,  $C_A \approx 1$ , and to increase as  $C_A \simeq \frac{1}{2} \frac{\beta_p}{1 + \beta_p} (k_{\perp} \rho_i)^2$  for  $k_{\perp} \rho_p > 1$ , i.e., in the KAW regime this ratio strongly depends on  $\beta_p$ . In the WW regime, instead, this ratio does not depend on the beta and also increases as  $k_{\perp}^2$ :  $C_A \simeq 2(k_{\perp} \rho_i)^2$ . Qualitatively, the relation  $C_A^{\text{WW}} \gtrsim C_A^{\text{KAW}(\beta=1)} \gtrsim C_A^{\text{KAW}(\beta=0.2)}$  holds. From Figure 5 (middle panel), the behavior of  $C_A$  at  $\beta_p = 1$  is again consistent with predominantly Alfvénic/KAW-like fluctuations, whereas at  $\beta_p = 0.2$  the large-scale behavior is consistent with MS/WW-like fluctuations. Nevertheless, due to the fact that the above qualitative relation  $C_A^{(\beta=1)} \gtrsim C_A^{(\beta=0.2)}$  is recovered at high  $k_{\perp}$  and, in the same range, the  $C_p$  ratio for the  $\beta = 0.2$  case increases toward unity, a *partial* contribution of KAW-type fluctuations—but not dominant, as highlighted by the  $C_{\parallel}$  ratio, below—cannot be excluded in the low- $\beta$  regime. Note that the decrease of  $C_A$  at  $k_{\perp} d_p \gg 1$  is also consistent with a coupling with IB modes in both regimes (Groselj et al. 2017).

Finally, let us consider the magnetic compressibility,  $C_{\parallel}$  (Figure 5, bottom panel): Alfvénic fluctuations would have small magnetic compressibility for  $k_{\perp} \rho_p \ll 1$  that increases as one goes to smaller and smaller scales and, in the KAW regime, eventually settles to a  $\beta$ -dependent value of  $C_{\parallel} \simeq \beta_p / (1 + 2/\beta_p)$  at  $k_{\perp} \rho_p > 1$  (represented in the bottom panel of Figure 5 by the green and blue horizontal dotted lines for  $\beta_p = 1$  and  $\beta_p = 0.2$ , respectively). Conversely, MS fluctuations have generally higher magnetic compressibility than the Alfvénic counterpart at  $k_{\perp} \rho_p < 1$  and, in the whistler regime, should settle to a  $\beta$ -independent value of  $C_{\parallel} = k_{\perp} / 2k \lesssim 1/2$  at  $k_{\perp} \rho_p > 1$ . From Figure 5 (bottom frame), we see that the magnetic compressibility is consistent with Alfvénic/KAW-like fluctuations at  $\beta_p = 1$ , i.e., it is small at  $k_{\perp} \rho_p < 1$  and then it increases to the nearly constant value of  $C_{\parallel} \simeq \beta_i / (1 + 2/\beta_i) = 1/3$  expected for KAWs at  $k_{\perp} \rho_p > 1$ . The  $\beta_i = 0.2$  regime instead exhibits a magnetic compressibility that is higher than that expected for Alfvénic/KAW fluctuations throughout the whole  $k_{\perp}$  range, consistent with a mixture of MS-, WW-, and IB-type fluctuations (Groselj et al. 2017). Note that  $k_{\perp} d_e$  effects can also enhance the compressibility of KAWs (Chen & Boldyrev 2017), so, consistently with the previous ratios, there could be a non-negligible contribution of KAW-like fluctuations at  $k_{\perp} \rho_p \gg 1$  also in this low- $\beta$  regime. All of these results are qualitatively in agreement with previous analyses performed in 2D fully kinetic and hybrid-kinetic simulations (Ceri et al. 2016, 2017; Groselj et al. 2017).

## 5. Conclusions

We presented the first high-resolution simulations of 3D3V hybrid-kinetic turbulence including electron inertia effects (with  $m_p/m_e = 100$ ), ranging from MHD scales to (perpendicular) scales well below the ion gyroradius. Two plasma beta parameters have been investigated: an “intermediate”  $\beta_p = 1$  regime and a “low”  $\beta_p = 0.2$  case.

In both regimes, the spectral properties of the subproton turbulent cascade, such as its power laws and spectral anisotropy, and the intermittent behavior of the fluctuations are in good agreement with SW observations and with the picture of turbulence mainly concentrated within 2D sheet-like

structures presented in Boldyrev & Perez (2012). In particular, all the turbulent fluctuations show a subproton-scale anisotropy pattern of the type  $k_{\parallel} \sim k_{\perp}^{2/3}$  and, correspondingly, the magnetic energy spectrum exhibits power laws in perpendicular and parallel wavenumbers that are  $k_{\perp}^{-8/3}$  and  $k_{\parallel}^{-7/2}$  at  $\beta_p = 1$  (being slightly steeper in  $k_{\perp}$  and much steeper in  $k_{\parallel}$  for the low- $\beta$  case, roughly going as  $k_{\perp}^{-3}$  and  $k_{\parallel}^{-5}$ ). This scenario also has been supported by intermittent analysis, which revealed deviations from monofractality and a strongly intermittent behavior at the kinetic scales (the  $\beta_p = 0.2$  regime being slightly more intermittent than the intermediate- $\beta$  case).

Moreover, we find that the turbulent cascade is dominated by Alfvénic/KAW-type fluctuations at  $\beta_p = 1$ , whereas the low- $\beta$  case presents a more complex scenario suggesting the simultaneous presence of different types of fluctuations, including magnetosonic and whistler-like ones. This picture seems also to be supported by the differences in the parallel correlation length of the magnetic fluctuations between the two regimes, thus possibly indicating a different decorrelation mechanism along the mean field. Nevertheless, signatures that may be interpreted as ion-Bernstein modes emerge in both regimes, although further focused investigations are needed in order to clarify this point. The presence of IB fluctuations would indeed point to a link between kinetic turbulence, dissipation, and reconnection (Podesta 2012; Narita et al. 2016a), as also suggested by the spectral properties (Boldyrev & Perez 2012; Loureiro & Boldyrev 2017; Mallet et al. 2017).

The results presented here are in qualitative agreement with previous two-dimensional studies performed with fully kinetic and hybrid-kinetic simulations (Ceri et al. 2016, 2017; Groselj et al. 2017), although we stress that this scenario needs to include other important effects, such as the role of magnetic reconnection and the coupling with coherent structures (Ceri & Califano 2017; Franci et al. 2017). While the hybrid-kinetic model does not include all of the electron kinetic physics and larger resolutions would be needed to better separate the electrons and protons kinetic scales, i.e., with a realistic mass ratio, the results presented here have far-reaching implications in the context of SW turbulence, from a possible dependence of the kinetic-scale cascade on the plasma  $\beta$  parameter to the understanding of the fundamental processes at play in collisionless kinetic plasma turbulence.

The authors acknowledge valuable discussions with F. Pegoraro, L. Franci, S. Landi, E. Papini, D. Groselj, and C. H. K. Chen. S.S.C. and F.C. thank C. Cavazzoni (CINECA, Italy) for his essential contribution to the HVM code parallelization and performances. The simulations were performed at CINECA (Italy) under the IS CRA initiative (grant HP10BEANCY).

## ORCID iDs

Silvio Sergio Ceri  <https://orcid.org/0000-0003-0562-6574>  
 Sergio Servidio  <https://orcid.org/0000-0001-8184-2151>  
 Francesco Califano  <https://orcid.org/0000-0002-9626-4371>

## References

- Alexandrova, O., Carbone, V., Veltri, P., & Sorriso-Valvo, L. 2008, *ApJ*, **674**, 1153
- Bale, S. D., Kellogg, P. J., Mozer, F. S., Horbury, T. S., & Reme, H. 2005, *PhRvL*, **94**, 215002

- Boldyrev, S., Horaites, K., Xia, Q., & Perez, J. C. 2013, *ApJ*, **777**, 41
- Boldyrev, S., & Perez, J. C. 2012, *ApJL*, **758**, L44
- Bruno, R., & Carbone, V. 2013, *LRSP*, **10**, 2
- Cerri, S. S., & Califano, F. 2017, *NJPh*, **19**, 025007
- Cerri, S. S., Califano, F., Jenko, F., Told, D., & Rincon, F. 2016, *ApJL*, **822**, L12
- Cerri, S. S., Franci, L., Califano, F., Landi, S., & Hellinger, P. 2017, *JPIPh*, **83**, 705830202
- Chen, C., & Boldyrev, S. 2017, *ApJ*, **842**, 122
- Chen, C. H. K. 2016, *JPIPh*, **82**, 535820602
- Chen, C. H. K., Boldyrev, S., Xia, Q., & Perez, J. C. 2013, *PhRvL*, **110**, 225002
- Cho, J., & Lazarian, A. 2004, *ApJL*, **615**, L41
- Franci, L., Cerri, S. S., Califano, F., et al. 2017, arXiv:1707.06548
- Franci, L., Landi, S., Matteini, L., Verdini, A., & Hellinger, P. 2015, *ApJ*, **812**, 21
- Franci, L., Landi, S., Matteini, L., Verdini, A., & Hellinger, P. 2016, *ApJ*, **833**, 91
- Frisch, U. 1995, *Turbulence. The legacy of A. N. Kolmogorov* (Cambridge: Cambridge Univ. Press)
- Galtier, S., & Bhattacharjee, A. 2003, *PhPI*, **10**, 3065
- Gary, S. P., & Smith, C. W. 2009, *JGRA*, **114**, A12105
- Groelj, D., Cerri, S. S., Banon Navarro, A., et al. 2017, arXiv:1706.02652
- He, J., Tu, C., Marsch, E., & Yao, S. 2012, *ApJL*, **745**, L8
- Howes, G. G., Cowley, S. C., Dorland, W., et al. 2008, *JGRA*, **113**, A05103
- Howes, G. G., TenBarge, J. M., Dorland, W., et al. 2011, *PhRvL*, **107**, 035004
- Huang, S. Y., Hadid, L. Z., Sahraoui, F., Yuan, Z. G., & Deng, X. H. 2017, *ApJL*, **836**, L10
- Kiyani, K. H., Chapman, S. C., Sahraoui, F., et al. 2013, *ApJ*, **763**, 10
- Lele, S. K. 1992, *JCoPh*, **103**, 16
- Loureiro, N. F., & Boldyrev, S. 2017, arXiv:1707.05899
- Mallet, A., Schekochihin, A. A., & Chandran, B. D. G. 2017, arXiv:1707.05907
- Mangenev, A., Califano, F., Cavazzoni, C., & Travnicek, P. 2002, *JCoPh*, **179**, 495
- Matthaeus, W. H., Oughton, S., Osman, K. T., et al. 2014, *ApJ*, **790**, 155
- Mithaiwala, M., Rudakov, L., Crabtree, C., & Ganguli, G. 2012, *PhPI*, **19**, 102902
- Narita, Y., Gary, S. P., Saito, S., Glassmeier, K.-H., & Motschmann, U. 2011, *GeoRL*, **38**, L05101
- Narita, Y., Nakamura, R., Baumjohann, W., et al. 2016a, *AnGeo*, **34**, 85
- Narita, Y., Nakamura, R., Baumjohann, W., et al. 2016b, *ApJL*, **827**, L8
- Osman, K. T., Matthaeus, W. H., Gosling, J. T., et al. 2014, *PhRvL*, **112**, 215002
- Passot, T., & Sulem, P. L. 2015, *ApJL*, **812**, L37
- Perri, S., Goldstein, M. L., Dorelli, J. C., & Sahraoui, F. 2012, *PhRvL*, **109**, 191101
- Podesta, J. J. 2012, *JGRA*, **117**, A07101
- Roberts, O. W., Li, X., & Li, B. 2013, *ApJ*, **769**, 58
- Sahraoui, F., Goldstein, M. L., Belmont, G., Canu, P., & Rezeau, L. 2010, *PhRvL*, **105**, 131101
- Schekochihin, A. A., Cowley, S. C., Dorland, W., et al. 2009, *ApJS*, **182**, 310
- Servidio, S., Osman, K. T., Valentini, F., et al. 2014, *ApJL*, **781**, L27
- Servidio, S., Valentini, F., Califano, F., & Veltri, P. 2012, *PhRvL*, **108**, 045001
- Shaikh, D., & Zank, G. P. 2009, *MNRAS*, **400**, 1881
- Sorriso-Valvo, L., Carbone, V., Veltri, P., Consolini, G., & Bruno, R. 1999, *GeoRL*, **26**, 1801
- Stawicki, O., Gary, S. P., & Li, H. 2001, *JGR*, **106**, 8273
- Sulem, P. L., Passot, T., Laveder, D., & Borgogno, D. 2016, *ApJ*, **818**, 66
- Told, D., Jenko, F., TenBarge, J. M., Howes, G. G., & Hammett, G. W. 2015, *PhRvL*, **115**, 025003
- Valentini, F., Califano, F., & Veltri, P. 2010, *PhRvL*, **104**, 205002
- Valentini, F., Trávníček, P., Califano, F., Hellinger, P., & Mangenev, A. 2007, *JCoPh*, **225**, 753
- Vainshstein, S. I. 1973, *JETP*, **37**, 73